scientific reports



OPEN Advancing neutron imaging techniques to highest resolution with fluorescent nuclear track detectors

Abdul Muneem^{1,2,14⊠}, Junya Yoshida^{1,3,4™}, Takehiko R. Saito^{1,5,6™}, Hiroyuki Ekawa¹, Masahiro Hino⁷, Katsuya Hirota⁸, Go Ichikawa^{8,9}, Ayumi Kasagi^{1,10}, Masaaki Kitaguchi^{11,12}, Kenji Mishima^{8,12}, Jameel-Un Nabi¹³ & Manami Nakagawa¹

Neutron imaging is a nondestructive and noninvasive inspection technique with a wide range of potential applications. However, the fundamentals of this technique still need to be improved, one of which involves achieving micrometer scale or even better resolution, which is a challenging task. Recently, a high-resolution neutron imaging device based on fine-grained nuclear emulsions was developed. Although these detectors demonstrate exceptionally high resolutions, they have several limitations. Furthermore, these detectors require an additional chemical development process and are thus not reusable. To overcome these limitations, we investigated whether neutron imaging devices based on fluorescent nuclear track detectors were suitable for high-resolution neutron imaging. Fluorescent nuclear track detectors are reusable solid-state detectors that do not require additional chemical processing. A novel technique combining neutron imaging based on fluorescent nuclear track detectors with a neutron converter layer formed using ${}^{10}\mathrm{B}_4\mathrm{C}$ was developed with unprecedented resolution. The neutron imaging of a gadolinium-based grating with a periodic structure of 9 µm was performed using the proposed fluorescent nuclear track detector-based neutron imaging device, and the grating structure was successfully resolved. The measured resolution was $0.887 \pm 0.009 \mu m$, which is the 1σ 10–90% edge response obtained using optical images of the fluorescent nuclear track

Neutron imaging (NI) is a widely used non-destructive inspection technique that can spatially resolve the inner structures of materials. Neutrons are neutral particles that can interact directly with atomic nuclei. Unlike X-rays, the absorption and scattering cross sections of neutrons do not correlate with the atomic number¹. Higher attenuation was observed for some light nuclei, such as hydrogen, carbon, boron, and lithium, and for heavy nuclei, such as cadmium and gadolinium. Smaller attenuation was observed for some heavy nuclei, such as aluminum, silicon, titanium, and lead. Therefore, NI is a potent nondestructive and noninvasive technique for visualizing the distribution of a wide range of elements based on distinctions in their neutron attenuation coefficients². However, NI complements X-ray imaging in several ways. NI is particularly useful for examining objects with dense outer shells and inner structures composed of lighter materials. NI, which emerged as a viable

¹High Energy Nuclear Physics Laboratory, Cluster for Pioneering Research, RIKEN, Wako, Saitama 351-0198, Japan. ²GIK Institute of Engineering Sciences and Technology, Topi, Swabi, KP 23640, Pakistan. ³Department of Physics, Tohoku University, Sendai, Miyagi 980-8578, Japan. ⁴International Center for Synchrotron Radiation Innovation Smart (SRIS), Tohoku University, Sendai, Miyagi 980-8577, Japan. ⁵GSI Helmholtzzentrum für Schwerionenforschung GmbH, 64291 Darmstadt, Germany. 6Saitama University, Sakura-ku, Saitama 338-8570, Japan. ⁷Institute for Integrated Radiation and Nuclear Science, Kyoto University, Kumatori, Sennan-gun, Osaka 590-0494, Japan. ⁸High Energy Accelerator Research Organization (KEK), Tsukuba, Ibaraki 305-0801, Japan. ⁹Japan Proton Accelerator Research Complex (J-PARC) Center, Tokai, Ibaraki 319-1195, Japan. ¹⁰Graduate School of Artificial Intelligence and Science, Rikkyo University, Tokyo 171-8501, Japan. ¹¹Department of Physics, Nagoya University, Furo-cho, Chikusa, Nagoya 464-8601, Japan. ¹²Kobayashi-Maskawa Institute for Origin of Particles and the Universe (KMI), Nagoya University, Furo-cho, Chikusa, Nagoya 464-8601, Japan. ¹³University of Wah, Quaid Avenue, Wah Cantt, Punjab 47040, Pakistan. 14 Present address: Neutron Beam Technology Team, RIKEN Center for Advanced Photonics, Wako, Saitama 351-0198, Japan. [™]email: abdulmuneemphysics25(agmail.com; junya.yoshida.e5@tohoku.ac.jp; takehiko.saito@riken.jp

industrial inspection technique in the 1950s, has continued to be relevant in recent years. The NI technique has been used for various applications, as demonstrated in Refs.²⁻⁸. In recent decades, advanced NI techniques have been developed to explore the micro-structural properties of materials over large areas. For example, the Bragg-edge neutron transmission method has become a powerful analytical tool, enabled by the advent of pulsed neutron sources such as SNS, ISIS, and J-PARC⁹⁻¹². The development of compact accelerator-driven neutron sources has enabled the acquisition of data of sufficient quality in the wavelength range useful for Bragg-edge NI^{13-16} .

Although NI is a powerful imaging technique, developing a neutron detector with high spatial resolution, at the micrometer scale level or even better¹⁷⁻²³, with better detection efficiency¹⁷ and time resolution^{5,24} remains a challenge. The spatial resolution of NI has improved to a few micrometers¹⁷⁻²³. The most commonly used NI method involves the conversion of the shading field of neutron radiation into a visible light image using scintillators containing converters such as ⁶Li or ¹⁵⁷Gd^{23,25-27} The luminescence of a neutron capture event can be observed using a charge-coupled device (CCD) or complementary metal-oxide semiconductor (CMOS) via an optical system. A resolution of 2 μm was achieved²⁶. Recently, an NI technique based on a fine-grained nuclear emulsion (FGNE), which is essentially a charge-particle tracking detector combined with a neutron converter layer formed using ¹⁰B₄C, was introduced^{28,29}. The NI device based on the FGNE exhibits a spatial resolution of 0.945 \pm 0.004 μm . The spatial resolution is defined in terms of the 1σ diffuseness of the edges of the grayscale optical images of the grating slit with a periodic structure of 9 µm²⁹. High spatial resolution, along with the world's best precision, was achieved with the FGNE. This is promising for the use of tracking detectors in imaging applications. Although FGNEs exhibit a high spatial resolution, NI devices on FGNEs have some drawbacks²⁹. FGNE-based NI devices are not reusable, and post-irradiation chemical processing is required after each neutron exposure.

Developing an NI detector that has submicrometer scale spatial resolution and complements the FGNE is challenging. To overcome this challenge, fluorescent nuclear track detectors (FNTDs) are reasonable candidates for use as NI devices, FNTD-based NI devices have been envisioned in Ref.³⁰. FNTDs are luminescent solidstate detectors based on Al₂O₃:C,Mg crystals^{31,32}. To utilize these FNTD-based NI devices for applications with reasonably high track density, approximately 1×10^4 tracks in an area of $100 \times 100 \ \mu m^2$ are required. As discussed in Ref.³⁰, the reusability of FNTDs for NI applications was assessed through seven irradiationbleaching cycles. Therefore, a novel approach was developed to perform optical bleaching using ultraviolet laser light with a wavelength of 355 nm under the required track density conditions for imaging applications. FNTDs can be reused at least seven times for NI applications.

As the key feature of FNTDs, it is essential to examine their reusability before employing them in imaging applications. After assessing the reusability of FNTDs for imaging applications ³⁰, neutron irradiation experiments were performed using the FNTD at the low-divergence beam branch³³ of BL05 at the Materials and Life Science Experimental Facility (MLF) of the Japan Proton Accelerator Research Complex (J-PARC)³⁴. FNTDs can record the three-dimensional trajectories of charged particles as they travel through detectors, similar to FGNEs. FNTD was employed for cold/ultracold neutron detection. The new FNTD was combined with a neutron converter layer formed using enriched ¹⁰B₄C, as shown in Fig. 1a. A ¹⁰B nucleus present in the neutron-converter layer absorbs neutrons and emits two charged particles heading in opposite directions via the following process: 10 B + n \rightarrow ⁷Li + ⁴He. When one of the emitted ions passes isotropically through the FNTD, the trajectory of the charged particle is recorded in the FNTD as the track of the incident charged particle. These tracks can be imaged using high-resolution nondestructive readout systems based on confocal laser scanning microscopy

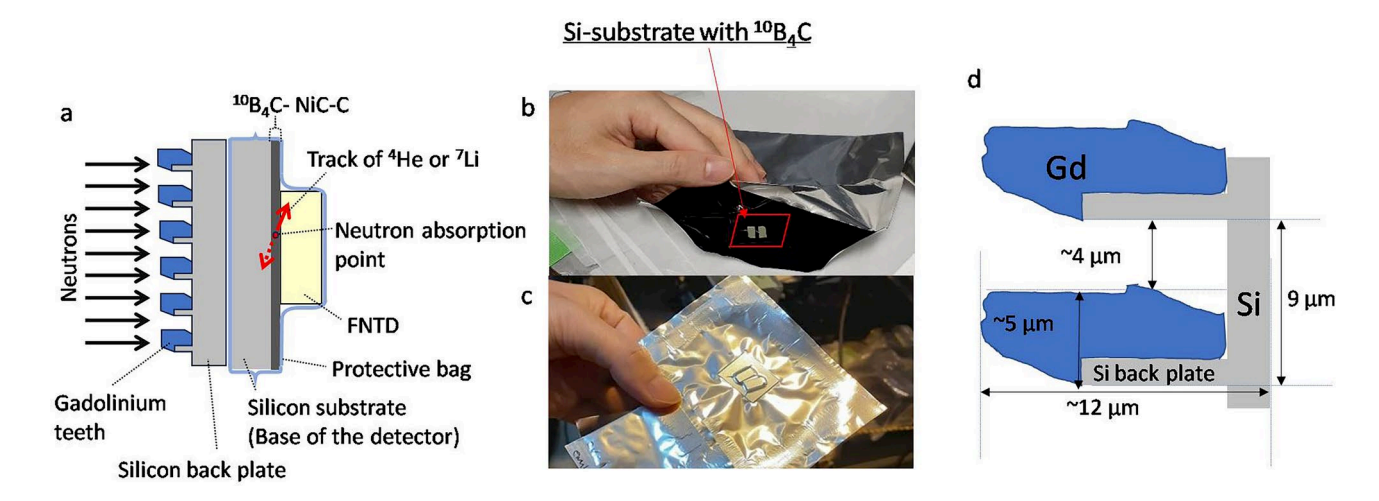


Fig. 1. Developed neutron detector with fluorescent nuclear track detector (FNTD). (a) Schematic layout of the neutron detector using an FNTD packed in a protective bag and a gadolinium-based grating. (b) FNTDs placed in a protective bag together with the enriched ¹⁰B₄C-based neutron converter. (c) FNTD-based neutron detector packed with light- and airtight laminated protective bag. (d) Schematic view of the two gadolinium teeth indicated as grating in (a).

Scientific Reports |

(CLSM)^{35,36}. The NI of a gadolinium-based grating with a periodic structure of 9 μ m was performed with the FNTDs using an approach similar to that in Refs.^{28,29}.

Results

The irradiated FNTDs were examined using CLSM. The FNTDs captured using a microscope (FV3000RS, Olympus) are shown in Fig. 3a. In this figure, the areas where the neutrons reach and emit tracks from the converter appear bright, whereas the regions where the neutrons are blocked appear dark. The periodic structure of the grating is successfully resolved. This is a benchmark result, as the NI of a micrometer-scale object was performed for the first time using FNTDs. A total of 52 images were acquired to evaluate the spatial resolution. The original image size is 1024×1024 pixels, as shown in Fig. 3a with dimensions of $106.07 \times 106.07 \, \mu \text{m}^2$. The images are resized to a resolution of 128×128 pixels as shown in Fig. 3b, to prevent correlation between the brightness of adjacent pixels as tracks span multiple pixels. The details of image processing are described in the "Methods" section, Resizing the images.

The sum of the brightness values of all pixels in the direction parallel to the grating edges (along the X-axis) is calculated as a function of pixel position along the Y-axis. The X- and Y-axes are shown in Fig. 3b. The red dotted lines in Fig. 3c display the peaks and valleys of the brightness sum graph, and these peaks and valleys are used as boundaries of each edge section. Using this process, 543 edges with peaks and valleys were deduced from the acquired 52 FNTD images. Examples of the deduced edges are shown in Fig. 4a,b.

Hirota et al. 28 concluded that developing algorithms and techniques for analyzing images under the accumulation of high track densities is essential for effectively utilizing FGNEs in imaging applications. A method for evaluating the spatial resolution using the brightness sum graph of a grating slit with a periodic structure utilizing an FGNE-based NI device was developed²⁹ under high track density conditions. Modulation transfer functions (MTF) and Gaussian error functions are commonly used to evaluate the imaging device resolution. However, in the present work and Ref.²⁹, the MTF was not suitable because the grating slit did not have a perfectly rectangular shape. The Gaussian error function was not suitable for evaluating the edge rise of the resolved grating edges in the acquired optical images. The flat plateau regions were not enough for applying the error function. Therefore, a trapezoidal fitting function was employed to evaluate the L(10-90%) edge response, as shown in Fig. 4a,b, to obtain the diffuseness distribution in a manner similar to the approach used in Ref.²⁹. Figure 4a,b show two examples of the trapezoid fitting of the extracted data points. Statistical error bars for each data point were calculated using the acquired FNTD images. The process of estimating the length of the statistical error bar is described in the "Methods" section, Estimation of the statistical error for trapezoidal fittings. A trapezoidal fitting function was employed to evaluate the edge response. The edge response, represented by the notation L (10-90%), is defined as the distance between 10 and 90% of the edges of the trapezoidal fitting curve. The dotted red lines in Fig. 4a,b represent the trapezoid fitting curves, and the blue dotted lines represent the point where the slope of the fitting curve changes. The legends of Fig. 4a,b indicate the distance of the slope of the fitting curve and reduced χ^2 value, which is an indicator of the goodness of employing a trapezoid fitting function. Figure 5a,b show the distribution of the L(10–90%) edge response and reduced χ^2 of the fitting for the 543 edges, respectively. The dotted red line in Fig. 5a show a Gaussian fitting curve. The mean value of the distribution of the 10-90% edge response (diffuseness) is $2.27 \pm 0.02 \mu m$ when employing a Gaussian fitting function. The deduced 1σ 10–90% edge response (imaging resolution) is 0.887 \pm 0.009 μm .

Discussion

In this paper, we present a novel NI device based on FNTDs combined with a neutron converter layer formed using $^{10}B_4C$. Experiments were performed to analyze the NI of a gadolinium-based grating of a known shape. For the first time, a micrometer-structured grating slit with a periodic structure of 9 μm was successfully resolved using the proposed NI technique. The NI with the FNTDs exhibited an unprecedented resolution of 0.887 \pm 0.009 μm . We conclude that a submicrometer-scale spatial resolution can be achieved using the proposed NI technique-based FNTDs. The spatial resolution was deduced using a comparable method, that is, the NI of a similar grating was performed using the FGNE, which exhibited a resolution of 0.945 \pm 0.004 μm^{29} . For a fair comparison between the two NI imaging devices based on FNTD and FGNE, trapezoidal fitting was used in this study and in Ref. Hence, it can be concluded that NI with FNTD is similar to or slightly better than that with FGNE. The deduced resolution is an inclusive assessment that comprises the effects of the resolution of the detector and shape of the gadolinium tooth, because the grating slit is not perfectly rectangular (Fig. 1d). The deduced resolution was determined to be the upper limit of the actual resolution. Therefore, FNTDs also demonstrate submicrometer spatial resolution for NI, which is comparable to that of FGNEs.

We investigated two NI detectors using $FGNE^{29}$ and FNTD (current study), both of which were combined with a neutron converter layer formed using $^{10}B_4C$. These detectors achieved submicrometer-scale spatial resolution. The FGNE-based NI devices require chemical processing for photographic development and cannot be reused. A dedicated optical microscope with an epi-illumination system was used to scan the emulsion layer, which could perform readings at speeds of up to 160 fps. However, FNTDs do not require developmental processing and can be reused at least seven times for NI applications 30 . However, CLSM was used to scan the FNTD, and it required approximately 1.5 min to capture a single microscopic image. Therefore, the development of high-speed confocal microscope-based scanners is required to employ FNTDs for imaging applications.

FNTDs are promising NI devices with numerous prospects for real-world applications. Because these detectors are reusable, optical bleaching can be performed when a high track density accumulates³⁰. However, the development of a compact automated optical bleaching system is crucial for further enhancing the user-friendliness of FNTDs.

Methods

Neutron detector with FNTDs

A schematic of the FNTD-based neutron detector developed in this study is presented in Fig. 1a. A 0.4 mm-thick silicon substrate was used as the base of the detector. 10 B₄C, NiC, and C layers with thicknesses of 230, 46, and 14 nm, respectively, were formed on a silicon substrate using an ion beam sputtering machine at the Institute for Integrated Radiation and Nuclear Science of Kyoto University³⁷. The thickness of the 10 B₄C layer, determined by X-ray reflectometry, was 230 nm, with a sputtering time of approximately 3 h. The thickness of the 10 B₄C layer was determined based on its effect on neutron detection efficiency, physical stability, and imaging resolution. An NiC layer was formed on the 10 B₄C layer to retain its physical stability. A C layer was used to provide chemical protection for the NiC layer. After the neutron converter was developed, the FNTD, a single crystal of aluminum oxide doped with carbon and magnesium, was combined with it, as shown in Fig. 1b. This study used a new FNTD measuring 8.0 × 4.0 × 0.5 mm³ in size, consisting of a single crystal produced by Landauer Inc. (Landauer Crystal Growth Division, Stillwater, OK, USA). The FNTD has a large polished surface that closely adheres to the neutron converter on the silicon substrate. The neutron detector was packed in moisture-proof, light-, and airtight-laminated bags composed of nylon, polyethylene, aluminum, polyethylene, and black polyethylene layers with thicknesses of 15, 13, 7, 13, and 35 μ m, respectively. The neutron detector after the airtight packing is shown in Fig. 1c.

Test object: Gadolinium-based grating

A gadolinium-based grating with a periodic structure of 9 μ m, which was originally fabricated for a Talbot–Lau interferometer configured for neutron phase imaging³⁸, was used for the NI experiments with FNTDs. The grating structure is discussed in Ref.²⁹. The photograph of the gadolinium-based grating with dimensions of $20 \times 20 \text{ mm}^2$ is shown in Fig. 2a. The scanning electron microscopy (SEM) images of the gadolinium-based grating structure are shown in Fig. 2b,c. These images are also presented in Ref.²⁹. The grating features a periodic structure with gadolinium present and absent every 9 μ m and is fabricated on a silicon substrate. A schematic of a single gadolinium tooth is presented in Fig. 1d. Periodic gadolinium teeth $\approx 5 \mu$ m wide with empty spaces of $\approx 4 \mu$ m, were fabricated on a 525- μ m thick silicon substrate. As shown in Fig. 1d, the gadolinium teeth are not perfectly rectangular owing to the production process^{39,40}. However, this structure was selected because it was the finest one available among the test objects that could be obtained. This grating can facilitate an inclusive assessment of diffuseness, accounting for both the resolution of the detector and the imperfect rectangular shape of the gadolinium teeth. This grating was also utilized for the spatial resolution evaluation of NI with FGNE, as detailed in Ref.²⁹.

During the NI experiments, the detector and grating were placed close to each other (Fig. 1a) to minimize the blurring effects induced by the spreading of the transmitted neutron beam. The neutron beam irradiated from left to right, as shown in Fig. 1a. Some incident neutrons were absorbed by the teeth, whereas the remaining neutrons passed through the empty spaces of 4 μ m and were absorbed in the 10 B₄C layer. Fig. 3a shows the

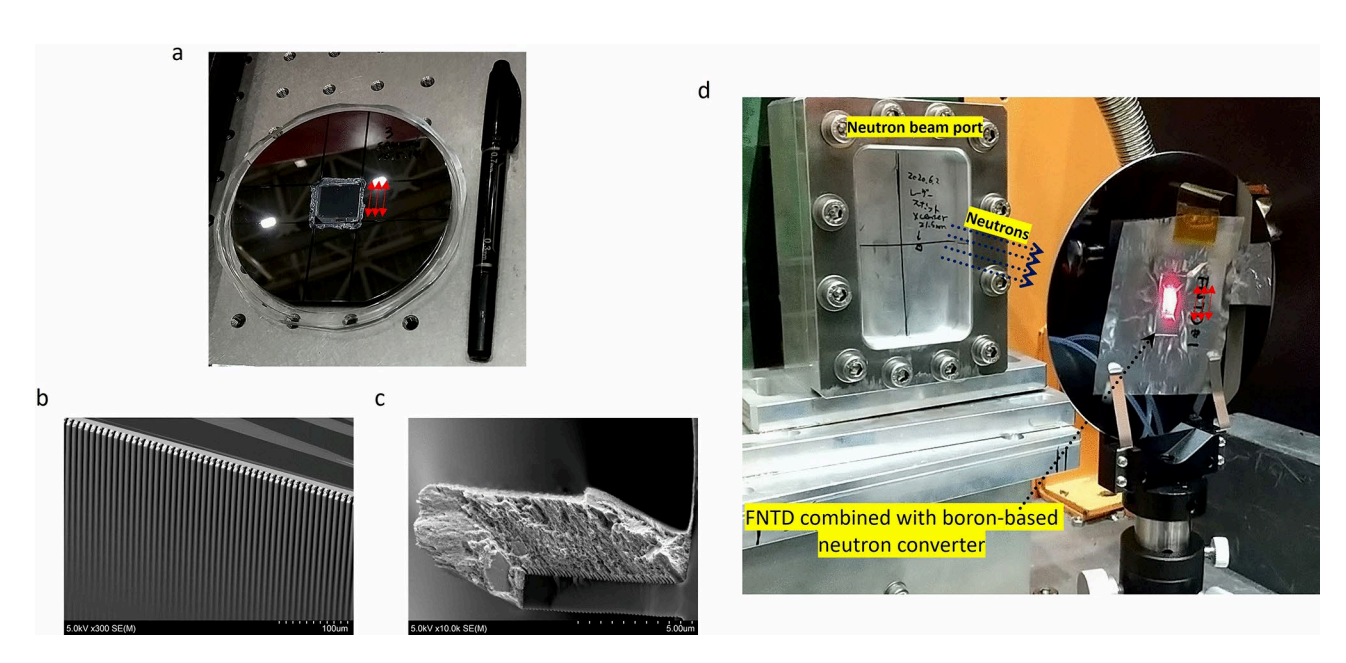


Fig. 2. Photographs of the gadolinium-based grating and layout of the neutron detector, showing a FNTD packed in a protective bag and combined with a gadolinium-based grating. (a) Photograph of the gadolinium-based grating with dimensions of $20 \times 20 \text{ mm}^2$. (b) Scanning electron microscopy (SEM) image showing the structure of the gadolinium teeth. (c) SEM image showing the cross-section of a single gadolinium tooth. (d) A photograph of the packed FNTD, combined with a boron-based neutron converter (Fig. 1a,b), placed in the low-divergence beam branch of BL05 at the MLF in J-PARC for neutron irradiation. The red arrows indicate the orientation of the gadolinium-based grating, as shown in (a).

microscopic image of the FNTD that recorded the tracks through the grating during neutron capture events. The dimensions and number of pixels in this image were $106.07 \times 106.07 \ \mu m^2$ and 1024×1024 , respectively. The structure of the gadolinium grating, with a periodicity of 9 μm , was successfully resolved for the first time. It was clearly visible in Fig. 3a.

Neutron imaging experiment

The NI of the grating was performed at the low-divergence beam branch 33 of BL05 in the MLF at J-PARC 34 . This beam branch is one of the most suitable branches in the MLF for this experiment because it can provide a reasonably intense neutron beam owing to its coupled neutron moderator. For the NI experiment, the aperture of the slit was set to 44 and 6 mm in the horizontal and vertical directions, respectively. The beam divergence in the horizontal and vertical directions was set to 0.3 and 10 mrad, respectively. Note that beam divergence in the direction parallel to the grating does not affect the image blurring. The direction of the gadolinium-based grating slit is indicated by the red arrows in Fig. 2a,d. The neutron flux was $2\times10^6~\text{n/cm}^2/\text{s}$, and the neutron irradiation time was set to 2.8 h to accumulate approximately $2\times10^4~\text{tracks per}~(100~\text{µm})^2$. The distance between the grating and $^{10}\text{B}_4\text{C}$ layer was 1.5 mm, which was equal to the combined thickness of the substrate and protective bag. The detector and grating were mechanically fixed using metal clips, mounted on a holder for the optical elements, and placed on an optical table, as shown in Fig. 2d. Beam irradiation was performed at a stable environmental temperature of 23.9 \pm 0.1 $^{\circ}\text{C}$.

Readout of the FNTD

FNTD readout was conducted using CLSM. The microscope (FV3000RS, Olympus) employed a fiber-optic laser with a wavelength of 640 nm, and the light was focused at a specific point within the FNTD using an objective lens. The excitation light at a wavelength of 750 nm was focused through an objective lens and detected using a photomultiplier tube. An oil objective lens with a high numerical aperture (NA) (Olympus UPlanFL N 40x/1.30NA) was used for the observation. The field depth was derived as $2\times\lambda$ / NA $^2\simeq0.89~\mu m$. A galvanometer scanner was used to scan the focal point within the FNTD in a two dimensions. The dimension of a single field of view, pixel number, and exposure time per pixel were set to 106.07 \times 106.07 μm^2 , 1024 pixels \times 1024 pixels, and 80 μs , respectively. These settings are among the preset values in the microscope scanning program. The laser intensity was approximately 0.2 mW.

For each field of view, at the beginning of the readout process, we defined the surface position of the FNTD by adjusting the focal plane and checking the excitation light emitting from the FNTD. The images were acquired by altering the depth in increments of $0.5~\mu m$ from the surface position. Among the obtained images, a superimposed image composed of four layers from the surface was used.

The FNTD was scanned on two different days. During the first and second read-outs, 16 and 36 images were acquired, respectively. To prevent an overlap in the field of view, the imaging position was shifted by 200 μ m, and 52 images were acquired for analysis. Given that the grating period is 9 μ m, approximately 12 cycles of the pattern were visible in each image. After obtaining the image dataset, we estimated the misalignment in angular deviations of the resolved grating edges in the FNTD images as 5.3 and 7.5 mrad for the 16 and 36 images, respectively. The misalignment distance in the images were 1700 and 1200 μ m for the 16 and 36 images, respectively. This effect was negligible for the subsequent analyses, and was not considered to avoid artificial broadening.

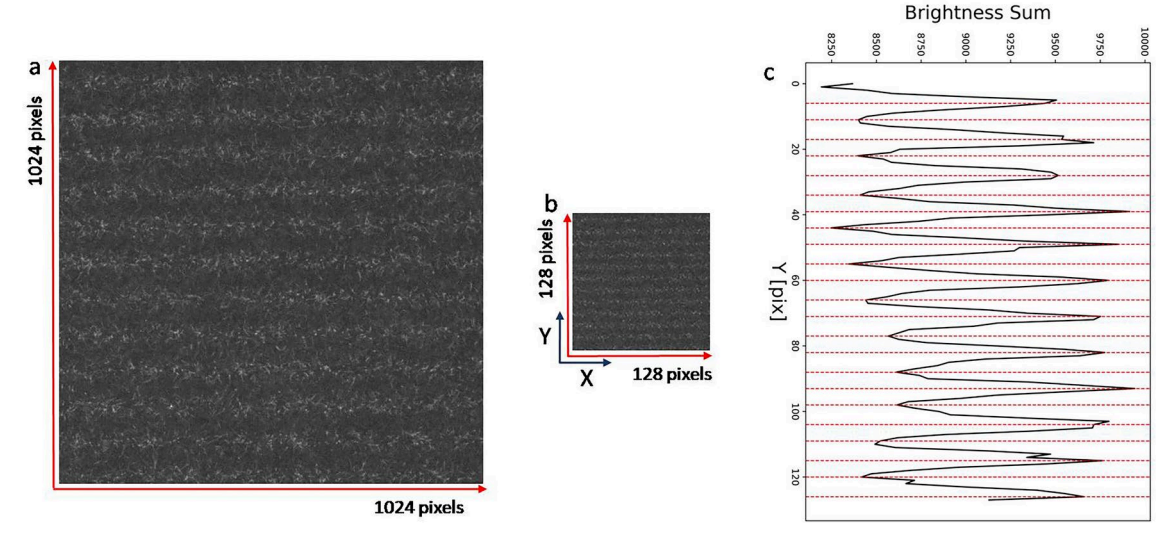


Fig. 3. (a) Microscopic image of the FNTD showing the recorded tracks during neutron capture events through the gratings. (b) Resized image of (a). (c) Brightness sum along the direction parallel to the grating (X-direction) as a function of the Y position in the resized FNTD image. The red dotted lines indicate the positions of the peaks and valleys and defined boundaries of individual edge sections.

Resizing the images

In the subsequent analyses, the FNTD images were scaled down from the original 1024×1024 pixels to 128×128 pixels using the nearest neighbor method⁴¹. Resizing of the FNTD images is crucial because of the occurrence of single tracks spanning multiple pixels, which causes a correlation between the brightness of neighboring pixels in the original images. FNTDs are based on Al_2O_3 :C,Mg crystals^{31,32}, and the trajectory of charged particles in the FNTD appears as bright fluorescence (also known as a "fluorescent track"), whereas in the case of FGNE, the trajectory of the charged particle can be recognized as a series of silver grains. In a previous analysis of the FGNE²⁹, optical images of 1024×1024 pixels (dimensions: $56 \times 56 \,\mu\text{m}^2$) were scaled down to 188 pixels $\times 188$ pixels using the nearest neighbor method⁴¹ such that the size of one pixel was equivalent to $0.3 \,\mu\text{m}$, which is the typical diameter of a developed silver grain. However, resizing FNTD images is not as straightforward as resizing FGNE images, because the resizing factor cannot be calculated from the characteristics of the FNTD.

The following procedure was used to estimate the correlation between the brightness of neighboring pixels: Fig. 6a,b show the FNTD image and its brightness sum along the X direction (as indicated in Fig. 6a), respectively. Figure 7a shows the average of the differences between the brightness sum values of pixels separated by Δx columns as a function of Δx . The error bars represent the corresponding standard deviation of the brightness sum values between pixels, and are shown in Fig. 7b. As indicated by the black arrow in the figure, pixels located closer than eight pixels, corresponding to 0.83 μm , exhibit correlation and should therefore be merged into a single pixel to eliminate brightness correlations.

Estimation of the statistical error for trapezoidal fittings

As discussed in the Results section, a trapezoidal fitting function was employed (Fig. 4a,b) to obtain the 10–90% edge response and assess the diffuseness. Figure 5a shows the distribution of the 10–90% edge response and diffuseness calculated by employing a Gaussian fitting function. However, as shown in Fig. 4a,b each data point of the brightness sum has a corresponding error bar. The procedure used to estimate the statistical error for each data point in this study differed from that discussed in Ref.²⁹. As discussed in Ref.²⁹, the statistical error bars were estimated using datasets of simulated images under various track density conditions. The mean and standard deviation were calculated from the brightness sum distribution of the resized simulated images. The deduced standard deviations were used as the error bar lengths for the corresponding brightness values. However, in the case of FNTDs, generating simulated images with background fluorescence is challenging because the track length of the charged particles and the structural appearance of the fluorescence tracks are unknown. Therefore, we employed a technique that uses FNTD images to estimate the corresponding error bars for each data point of the brightness sum, as shown in Fig. 4a,b. The following procedure was used to estimate the error bar for each data point of the brightness sum.

First, FNTD images were scaled down from their original size of 1024×1024 pixels to 128×128 pixels. The projection of the sum of brightness values of the resized FNTD images is shown in Fig. 8a. We extracted pixel rows at 9 μ m intervals from the actual striation patterns. In Fig. 8a, the red lines indicate a total of 10 pixel rows, numbered from 1 to 10. For each pixel row, the mean values of the sum of brightness were extracted for the regions indicated by the circles in Fig. 8a. The deduced mean values are indicated by the corresponding values (Fig. 8a) and circles as shown in Fig. 8b. The mean and standard deviation values were calculated from the ten data points obtained, as shown in Fig. 8b. This process was repeated for the next 10 consecutive pixel rows to scan all brightness sum values for the peaks and valleys. The other 10 figures correspond to the next 10 consecutive portions of the FNTD image, as shown in Fig. 8 in Supplementary Material (Supplementary Figs. S1–S10). Figure 9a displays the summary of the mean values of the brightness sum for 11 regions in a single FNTD image. The error bars for the corresponding standard deviations are shown in Fig. 9b. This process was iterated for all 52 FNTD images acquired, and all standard deviation values were accumulated, as shown in Fig. 10. The resulting

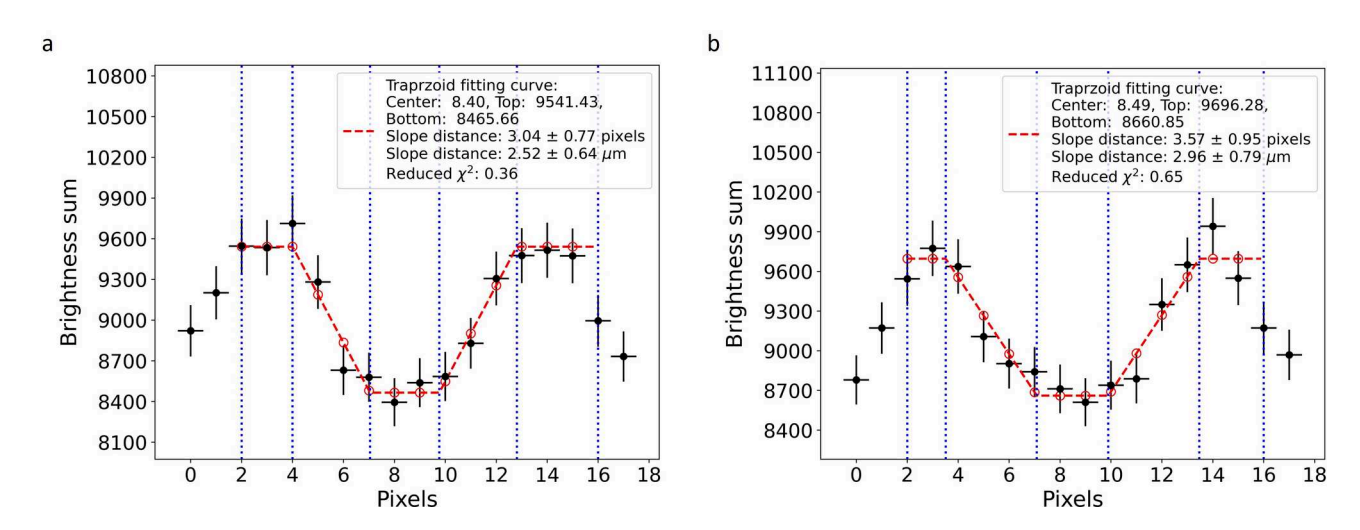


Fig. 4. (**a,b**) Two examples of data points of the brightness sum for two pair of rising and falling edges, from Fig. 3c and trapezoid fitting. The red dotted lines represent the trapezoid fitting curve.

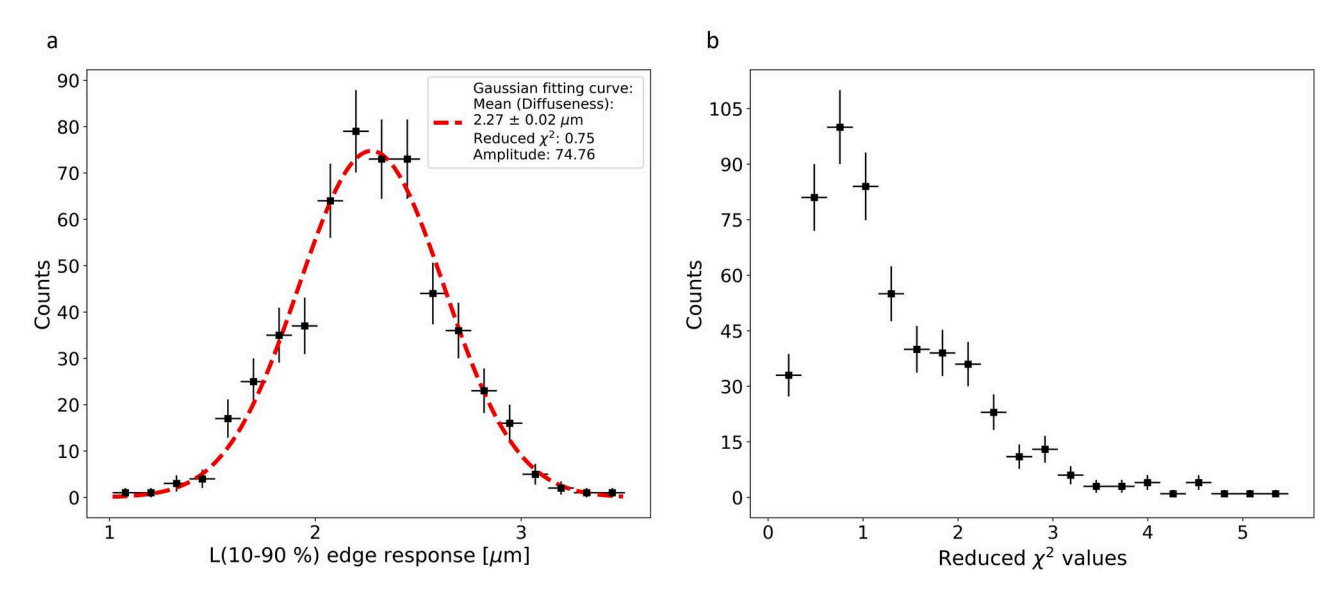


Fig. 5. Distribution of the **(a)** L(10–90%) edge response for 543 striations from 52 FNTD images. **(b)** Reduced χ^2 values for the fitting with the trapezoid fitting function.

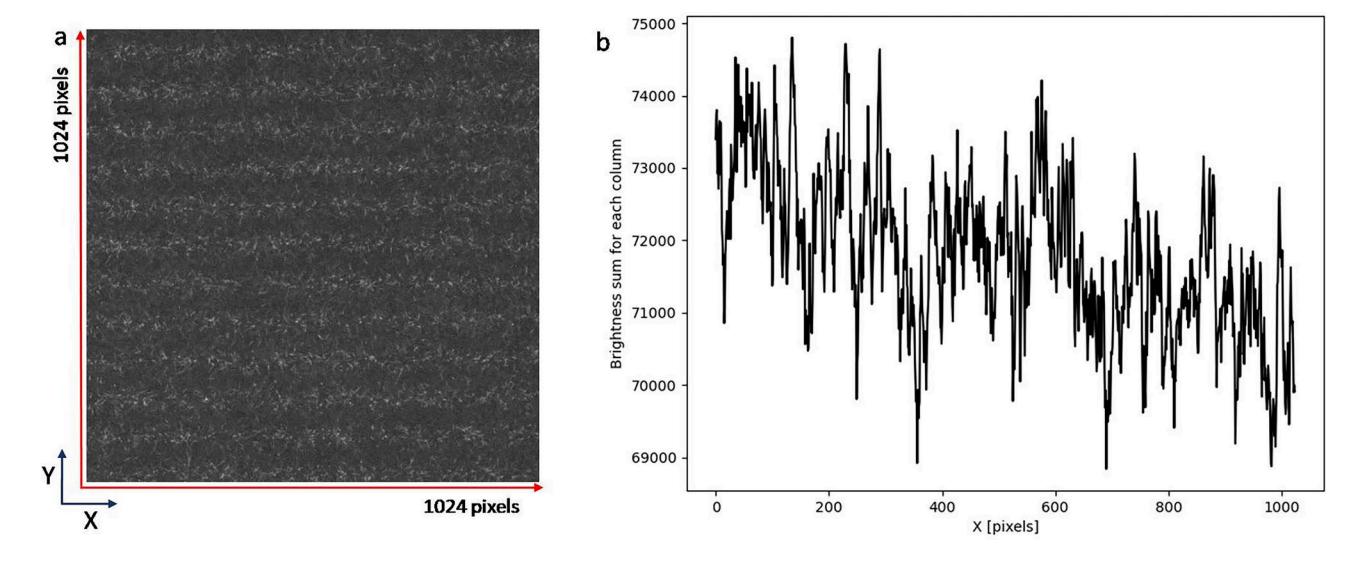


Fig. 6. (a) FNTD image of the neutron detector after the neutron imaging (NI) experiment, identical to that in Fig. 2. (b) Brightness sum along the Y direction in the FNTD image, as indicated in (a).

data points for the standard deviation were fitted using a linear function. From the fitting, the linear function Y = 0.0234X - 19.5959 (Fig. 10) was obtained and used to estimate the error bar for the trapezoidal fitting.

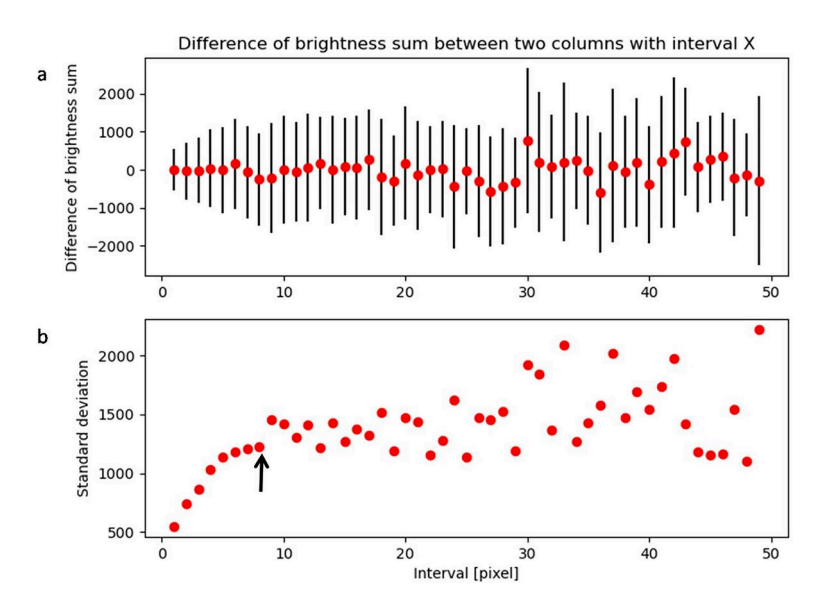


Fig. 7. (a) Brightness difference between two rows at a specified interval of the brightness sum projection, as shown in Fig. 6b, under defined intervals ranging from 1 to 50. (b) Standard deviation of the brightness difference under the given interval range. As indicated by a black arrow, pixels located closer than eight pixels, corresponding to $0.83 \mu m$, exhibit correlation.

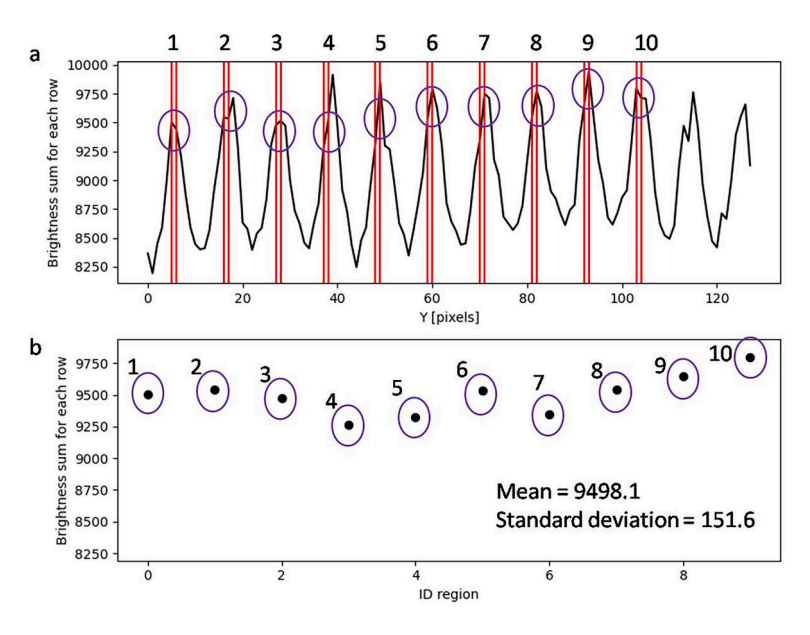


Fig. 8. (a) Brightness sum projection of an FNTD image. The red lines show the region of first pixel rows at 9 mm intervals from the actual striation patterns. The mean and standard deviation were calculated in the given portion, indicated by the red lines. (b) Data points representing the calculated mean and standard deviation values in each region. The mean and standard deviation values of the 10 data points are 9498.1 and 151.6, respectively.

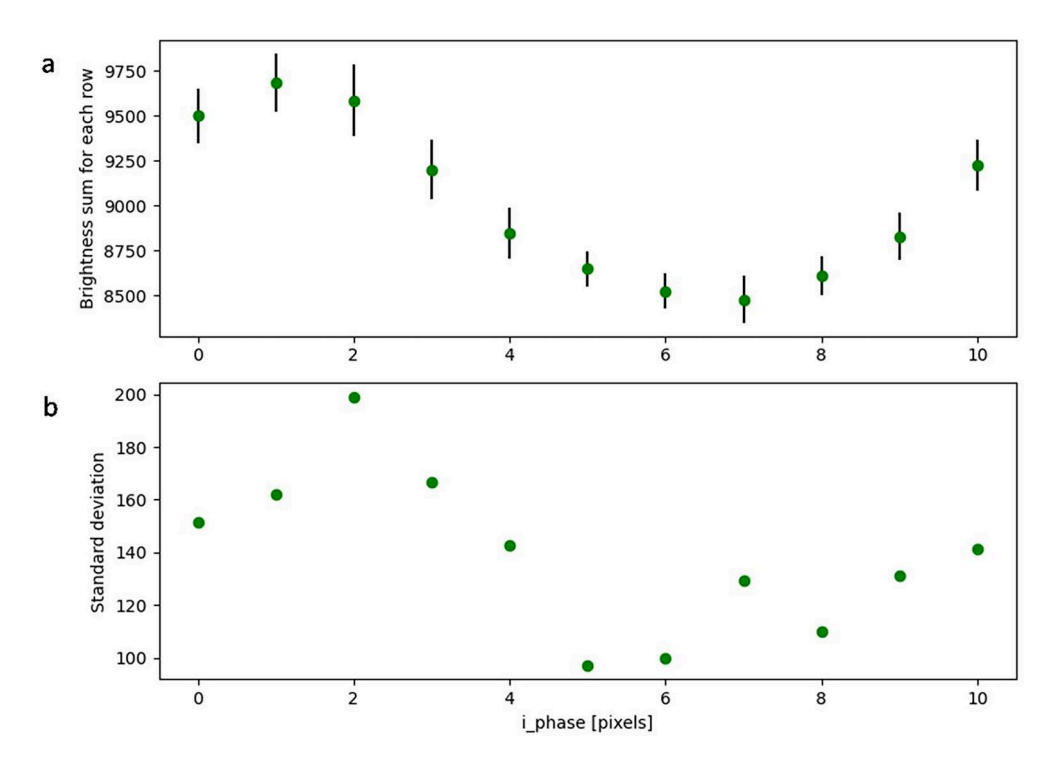


Fig. 9. (a) Summary of the mean values of the brightness sum for 11 regions. Each FNTD image was divided into 11 portions. (b) Summary of the standard deviation for a single FNTD image.

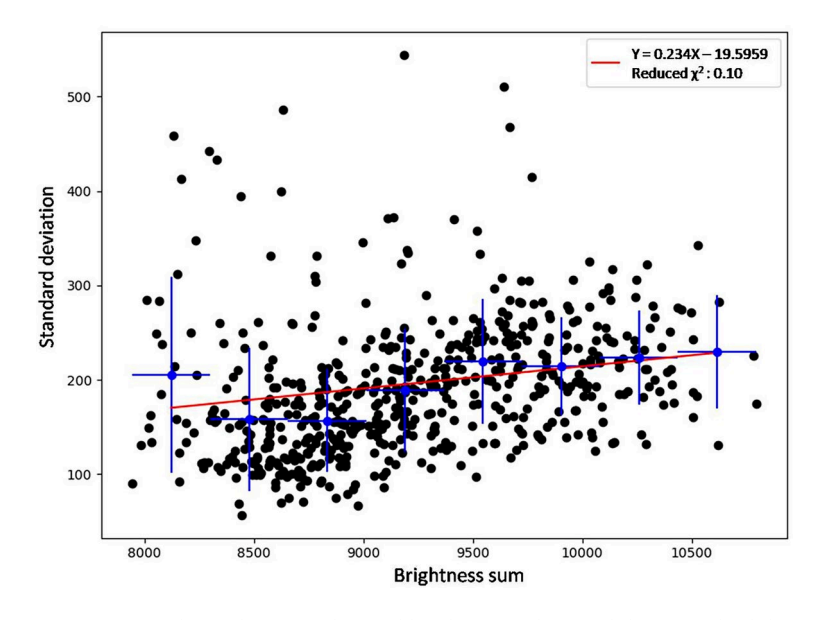


Fig. 10. Correlation between the total brightness values and their standard deviation. The data points obtained for all 52 FNTD images were accumulated. The blue data points with error bars represent the calculated average and standard deviation of the data points within each of the divided regions. A red line indicates the linear function fitting line.

Data availability

The data supporting the findings of this study are available from the corresponding author upon request.

Code availability

Computer codes supporting the findings of this study are available from the corresponding author upon request.

Received: 3 July 2024; Accepted: 24 December 2024

Published online: 24 January 2025

References

- 1. Banhar, J. Advanced Tomographic Methods in Materials Research and Engineering (Oxford University Press, 2008).
- 2. Strobl, M. et al. Topical review: Advances in neutron radiography and tomography. J. Phys. D Appl. Phys. 42, 243001. https://doi.o g/10.1088/0022-3727/42/24/243001 (2009)
- 3. Hussey, D. S. & Jacobson, D. L. Applications of neutron imaging and future possibilities. Neutron News 26, 19-22. https://doi.org/ 10.1080/10448632.2015.1028273 (2015).
- 4. Lehmann, E. H., Boillat, P., Kaestner, A., Vontobel, P. & Mannes, D. Neutron imaging methods for the investigation of energy related materials. EPJ Web Conf. 104, 01007. https://doi.org/10.1051/epjconf/201510401007 (2015).
- 5. Kardjilov, N., Manke, I., Woracek, R., Hilger, A. & Banhart, J. Advances in neutron imaging. Mater. Today 21, 652-672. https://do i.org/10.1016/j.mattod.2018.03.001 (2018).
- 6. Tengattini, A., Lenoir, N., Andò, E. & Viggiani, G. Neutron imaging for geomechanics: A review. Geomech. Energy Environ. 27, 100206. https://doi.org/10.1016/j.gete.2020.100206 (2021).
- 7. Song, B. et al. Dynamic lithium distribution upon dendrite growth and shorting revealed by operando neutron imaging. ACS Energy Lett. 4, 2402-2408. https://doi.org/10.1021/acsenergylett.9b01652 (2019).
- 8. Ly, S. et al. Operando monitoring the lithium spatial distribution of lithium metal anodes. Nat. Commun. 9, 2152. https://doi.org/ 10.1038/s41467-018-04394-3 (2018).
- 9. Gabriel, T. A., Haines, J. R. & McManamy, T. J. Overview of the spallation neutron source (sns) with emphasis on target systems. J. Nucl. Mater. 318, 1-13. https://doi.org/10.1016/S0022-3115(03)00010-2 (2003).
- Thomason, J. The isis spallation neutron and muon source-the first thirty-three years. Nucl. Instrum. Methods Phys. Res. Sect. A 917, 61-67. https://doi.org/10.1016/j.nima.2018.11.129 (2019).
- 11. Arai, M. & Maekawa, F. Japan spallation neutron source (jsns) of j-parc. Nucl. Phys. News 19, 34-39. https://doi.org/10.1080/1050 6890903405316 (2009).
- 12. Shinohara, T. et al. The energy-resolved neutron imaging system, RADEN. Rev. Sci. Instrum. 91, 043302. https://doi.org/10.1063/ 1.5136034 (2020).
- 13. Furusaka, M., Sato, H., Kamiyama, T., Ohnuma, M. & Kiyanagi, Y. Activity of Hokkaido university neutron source, huns. Phys. Procedia 60, 167-174. https://doi.org/10.1016/j.phpro.2014.11.024 (2014).
- 14. Otake, Y. Applications of Laser-Driven Particle Acceleration (2018).
- 15. Leuschner, M. et al. Lens: A new university-based neutron source for science and education. Nucl. Instrum. Methods Phys. Res. Sect. B Beam Interact. Mater. Atoms 261, 956-959. https://doi.org/10.1016/j.nimb.2007.03.108 (2007).
- 16. Kino, K. et al. Design of a compact electron accelerator-driven pulsed neutron facility at aist. Nucl. Instrum. Methods Phys. Res. Sect. A 927, 407-418. https://doi.org/10.1016/j.nima.2019.02.062 (2019).
- 17. Tremsin, A. et al. Improved efficiency of high resolution thermal and cold neutron imaging. Nucl. Instrum. Methods Phys. Res. Sect. A 628, 415–418. https://doi.org/10.1016/j.nima.2010.07.014 (2011).
- 18. Hussey, D. et al. A new cold neutron imaging instrument at nist. Phys. Procedia 69, 48-54. https://doi.org/10.1016/j.phpro.2015.0 7 006 (2015)
- 19. Trtik, P. et al. Improving the spatial resolution of neutron imaging at Paul Scherrer Institut—The neutron microscope project. Phys. Procedia 69, 169-176. https://doi.org/10.1016/j.phpro.2015.07.024 (2015).
- 20. Trtik, P. & Lehmann, E. H. Progress in high-resolution neutron imaging at the Paul Scherrer Institut—The neutron microscope project. J. Phys. Conf. Ser. 746, 012004. https://doi.org/10.1088/1742-6596/746/1/012004 (2016).
- 21. Bingham, P., Santos-Villalobos, H., Lavrik, N., Gregor, J. & Bilheux, H. Magnified neutron radiography with coded sources. Phys. Procedia 69, 218-226. https://doi.org/10.1016/j.phpro.2015.07.031 (2015).
- 22. Morgano, M. et al. Unlocking high spatial resolution in neutron imaging through an add-on fibre optics taper. Opt. Express 26, 1809-1816. https://doi.org/10.1364/OE.26.001809 (2018).
- 23. Trtik, P. et al. PSI neutron microscope at ILL-D50 beamline—First results. Mater. Res. Proc. 15, 23-28. https://doi.org/10.21741/9 781644900574-4 (2020).
- 24. Woracek, R. et al. Spatially resolved time-of-flight neutron imaging using a scintillator cmos-camera detector with kHz time resolution. Opt. Express 27, 26218-26228. https://doi.org/10.1364/OE.27.026218 (2019).
- 25. Lehmann, E. H. et al. Neutron imaging—Detector options in progress. J. Instrum. 6, C01050. https://doi.org/10.1088/1748-0221/6 /01/c01050 (2011).
- 26. Hussey, D. S., LaManna, J. M., Baltic, E. & Jacobson, D. L. Neutron imaging detector with 2 m spatial resolution based on event reconstruction of neutron capture in gadolinium oxysulfide scintillators. Nucl. Instrum. Methods Phys. Res. Sect. A 866, 9-12. https://doi.org/10.1016/j.nima.2017.05.035 (2017).
- 27. Jiang, X. et al. Study on the neutron imaging detector with high spatial resolution at china spallation neutron source. Nucl. Eng. Technol. 53, 1942-1946. https://doi.org/10.1016/j.net.2020.12.009 (2021).
- Hirota, K. et al. Neutron imaging using a fine-grained nuclear emulsion. J. Imaging 7, 4. https://doi.org/10.3390/jimaging7010004 (2021).
- 29. Muneem, A. et al. Investigation of neutron imaging applications using fine-grained nuclear emulsion. J. Appl. Phys. 133, 054902. https://doi.org/10.1063/5.0131098 (2023).
- 30. Muneem, A. et al. Study on the reusability of fluorescent nuclear track detectors using optical bleaching. Radiat. Meas. 158, 106863. https://doi.org/10.1016/j.radmeas.2022.106863 (2022).
- 31. Akselrod, M. S. & Akselrod, A. E. New Al₂O₃:C, Mg crystals for radiophotoluminescent dosimetry and optical imaging. Radiat. Prot. Dosim. 119, 218–221. https://doi.org/10.1093/rpd/nci663 (2006).
- 32. Akselrod, M. & Kouwenberg, J. Fluorescent nuclear track detectors—Review of past, present and future of the technology. Radiat. Meas. 117, 35-51. https://doi.org/10.1016/j.radmeas.2018.07.005 (2018).
- 33. Mishima, K. et al. Design of neutron beamline for fundamental physics at J-PARC BL05. Nucl. Instrum. Methods Phys. Res. Sect. A 600, 342-345. https://doi.org/10.1016/j.nima.2008.11.087 (2009).
- 34. Nakajima, K. et al. Materials and life science experimental facility (mlf) at the Japan proton accelerator research complex ii: Neutron scattering instruments. Quantum Beam Sci. 1, 1 (2017).
- 35. Akselrod, G. et al. A novel al203:c, mg fluorescent nuclear track detector for heavy charged particles and neutrons. Nucl. Instrum. Methods Phys. Res. Sect. B Beam Interact. Mater. Atoms 247, 295-306. https://doi.org/10.1016/j.nimb.2006.01.056 (2006).
- 36. Akselrod, M. S. et al. Automatic neutron dosimetry system based on fluorescent nuclear track detector technology. Radiat. Prot. Dosim. 161, 86-91. https://doi.org/10.1093/rpd/nct293 (2013).
- 37. Hino, M. et al. The ion beam sputtering facility at KURRI: Coatings for advanced neutron optical devices. Nucl. Instrum. Methods Phys. Res. Sect. A 797, 265-270. https://doi.org/10.1016/j.nima.2015.06.046 (2015).
- Seki, Y. et al. Experimental evaluation of neutron absorption grating fabricated by oblique evaporation of gadolinium for phase imaging. Phys. Procedia 88, 217-223. https://doi.org/10.1016/j.phpro.2017.06.030 (2017)
- Samoto, T., Takano, H. & Momose, A. Gadolinium oblique evaporation approach to make large scale neutron absorption gratings for phase imaging. Jpn. J. Appl. Phys. 58, 12. https://doi.org/10.7567/1347-4065/ab138d (2019).

Scientific Reports |

- Samoto, T., Takano, H. & Momose, A. Evaluation of obliquely evaporated gadolinium gratings for neutron interferometry by X-ray microtomography. *Mater. Sci. Semicond. Process.* 92, 91–95. https://doi.org/10.1016/j.mssp.2018.05.038 (2019).
- Rukundo, O. & Cao, H. Nearest neighbor value interpolation. Int. J. Adv. Comput. Sci. Appl. 3, 5. https://doi.org/10.14569/IJACSA.2012.030405 (2012).

Acknowledgements

The neutron experiments were conducted at MLF of the J-PARC using user programs (Proposal No. 2020B0223). Junya Yoshida received support from the JSPS KAKENHI Grant-in-Aid for Scientific Research on Innovative Areas 6005 (Grant Number JP18H05403). The authors express their gratitude to Yoshichika Seki of Tohoku University, Japan, for lending the gadolinium-based grating with known geometry. The authors also thank the RIK-EN CBS-EVIDENT Open Collaboration Center for their technical assistance with confocal image acquisition, and Yukiko Kurakata of the High Energy Nuclear Physics Laboratory at RIKEN for providing administrative support for this project.

Author contributions

Preparation of the experiment: AM, JY, KH, and KM. Conduction of the experiment: AM, JY, and KM. Data analysis: AM, JY, TRS, KH, KM, and AK. Discussion and manuscript preparation: AM, JY, TRS, HE, MH, KH, GI, AK, MK, KM, JN and MN. Project management: TRS.

Declarations

Competing interests

The authors declare no competing interests.

Additional information

Supplementary Information The online version contains supplementary material available at https://doi.org/10.1038/s41598-024-84591-x.

Correspondence and requests for materials should be addressed to A.M., J.Y. or T.R.S.

Reprints and permissions information is available at www.nature.com/reprints.

Publisher's note Springer Nature remains neutral with regard to jurisdictional claims in published maps and institutional affiliations.

Open Access This article is licensed under a Creative Commons Attribution-NonCommercial-NoDerivatives 4.0 International License, which permits any non-commercial use, sharing, distribution and reproduction in any medium or format, as long as you give appropriate credit to the original author(s) and the source, provide a link to the Creative Commons licence, and indicate if you modified the licensed material. You do not have permission under this licence to share adapted material derived from this article or parts of it. The images or other third party material in this article are included in the article's Creative Commons licence, unless indicated otherwise in a credit line to the material. If material is not included in the article's Creative Commons licence and your intended use is not permitted by statutory regulation or exceeds the permitted use, you will need to obtain permission directly from the copyright holder. To view a copy of this licence, visit http://creativecommons.org/licenses/by-nc-nd/4.0/.

© The Author(s) 2025